



# Nanostructured ceria-zirconia catalysts for CO oxidation: Study on surface properties and reactivity



Marco Piumetti, Samir Bensaid, Debora Fino, Nunzio Russo\*

Department of Applied Science and Technology, Politecnico di Torino, Corso Duca degli Abruzzi 24, 10129 Torino, Italy

## ARTICLE INFO

### Article history:

Received 24 November 2015

Received in revised form 1 February 2016

Accepted 7 February 2016

Available online 10 February 2016

### Keywords:

Cerium-zirconium oxides

CO oxidation

Properties of cerium based oxides

Nanostructured ceria

Ceria-based catalysts

## ABSTRACT

In the present work, a set of Ce-Zr-O catalysts was prepared to study the effect of Zr-content (in the range 10–30 at.%) and the surface-dependency activity towards CO oxidation, a prototypical reaction for oxidation catalysis. The physico-chemical features of the prepared materials were investigated using complementary techniques.

As a whole, it was observed that the oxidation activity of ceria-zirconia nanocatalysts mainly depends on the presence of (100) and (110) crystalline planes, thus confirming the structure-sensitivity for this reaction over Ce-Zr mixed oxides. Moreover, the abundant population of carbonate-like species on more open and reactive surfaces has a beneficial effect on the reactivity of the Ce-Zr-O nanomaterials.

The best compromise between the structural defects and redox-active centres ( $\text{Ce}^{3+}/\text{Ce}^{4+}$  pairs) was observed for the most active nanocatalyst, namely the  $\text{Ce}_{0.9}\text{Zr}_{0.1}\text{O}_2-\text{NP}$  (nanopolyhedra with sizes of about 20–40 nm). The latter exhibited better CO conversion values compared to similar Ce-Zr-O nanocatalysts with higher Zr-contents (namely,  $\text{Ce}_{0.8}\text{Zr}_{0.2}\text{O}_2-\text{NP}$  and  $\text{Ce}_{0.7}\text{Zr}_{0.3}\text{O}_2-\text{NP}$ ). On the other hand, lower activities were obtained for the high-surface-area catalysts (e.g. mesostructured materials) with the same Ce/Zr ratio, thus showing the key role played by the structural features of solid catalysts for this reaction.

© 2016 Elsevier B.V. All rights reserved.

## 1. Introduction

Over the last few decades, ceria and ceria-based materials have received much interest as catalysts and catalytic supports for use in many oxidation reactions, including diesel soot combustion, CO oxidation and VOCs abatement [1–4]. The latter applications, indeed, take advantage of the unique redox properties and high oxygen storage capacity (OSC) of ceria. However, pure ceria is seldom used for oxidation processes, since it is known to have poor thermal stability [5]. Thus, the presence of isovalent non-reducible elements, such as  $\text{Zr}^{4+}$  cations, into the ceria lattice may have a favourable effect on the physico-chemical properties of ceria, improving its thermal stability, OSC, oxygen mobility in the solid framework, and so on [1,6]. Moreover, the substitution of  $\text{Ce}^{4+}$  cations with  $\text{Zr}^{4+}$  promotes the formation of structural defects (e.g. terraces, ledges and kinks) on the catalyst surface, with surface atoms having different coordination environments (namely, coordination numbers) [7]. Structural defects can favour the mobility of charged species, such as electrons or oxygen anions in the solid catalyst and are considered to be essential for generating cat-

alytic active species [3]. For this reason, over the last few decades, ceria-zirconia catalysts have been widely investigated for oxidation catalysis (i.e. soot combustion, CO oxidation, VOCs abatement, etc.) because of their interesting catalytic performances (redox behaviour) and high thermal stability, as shown in previous works [1–4,8]. It should be noted that defect sites and oxygen vacancies ( $\text{O}_v$ ) are among the most desirable active species for oxidation catalysis [8–10]. These structural defects modify the local electronic structure and can significantly impact the surface reactivity. According to the Volkenstein Electronic Theory [11], the presence of defect sites, associated with  $\text{O}_v$ , in fact modifies the Fermi Energy level, thus promoting the oxidation processes [12].

CO oxidation, a primary function of three-way catalytic converters (TWCs), Diesel Oxidation Catalysts (DOC) and Diesel Particulate Filters (DPF) containing ceria, can be a prototypical reaction for probing the catalytic oxidation activity of ceria-based catalysts [13–16]. Therefore, many experimental and theoretical studies have been devoted to understanding catalytic oxidation of CO by ceria, doped-ceria and related materials. According to the literature [1,13,16,17], CO oxidation over ceria-based catalysts takes place through a Mars-van Krevelen mechanism, whereby the reaction involves alternating reduction-oxidation steps on the solid surface with the formation of oxygen vacancies and their successive replenishment by gas-phase oxygen. During the first step, CO reacts with

\* Corresponding author.

E-mail address: [nunzio.russo@polito.it](mailto:nunzio.russo@polito.it) (N. Russo).

surface oxygen to produce  $\text{CO}_2$  and  $\text{O}_v$  (reduced catalyst surface). This reaction step is promoted by the excellent oxygen-buffering capacity of ceria, a property widely used in automotive catalysis [16]. In the second step, a molecule of  $\text{O}_2$  fills this  $\text{O}_v$ , thus restoring the catalyst surface (re-oxidation or self-repair mechanism).

Over the years, a general consensus has been reached on the fact that CO interaction with ceria is structure dependent [13,16]. It has been shown that small ceria particles (i.e. nanowires and nanorods), exhibiting an abundance of (110) and (100) facets, are catalytically more active toward several reactions than  $\text{CeO}_2$ -particles with preferred exposure of stable (111) planes [16,18–23].

Exposure of specific crystallographic facets, together with the increased number of edges, corners and facets is of critical importance in controlling the surface reactivity and, in addition, nanocatalysts with multifaceted morphologies are highly desirable in heterogeneous catalysis. For fcc structured metals, the surface energy density ( $\gamma$ ) for the three lowest index planes can be ranked as  $\gamma_{(111)} < \gamma_{(100)} < \gamma_{(110)}$  [24,25]. Experimental data confirmed that this trend may also hold for ceria-based materials [25]. Theoretical works on the interaction between CO and  $\text{CeO}_2$  surfaces have shown the structure-sensitivity for CO adsorption, predicting weak CO adsorption for the most stable (111) plane and stronger chemisorption with (100) and (110) surfaces [26–31]. In this scenario, the metastable ceria (110) surface seems to be the most promising candidate for CO oxidation, since the formation of oxygen vacancies on the (110) planes needs the least amount of energy [32]. Theoretical studies, indeed, have shown that the  $\text{O}_v$  formation energy depends on the nature of oxide surface [33,34]. On the other hand, it has been well established that the specific surface area of solid catalysts is a key factor in determining their overall catalytic activity in a wide number of (oxidation) reactions [3,4,35–37]. Therefore, it is necessary to maximize the dispersion of the nanoparticles using high-surface-area supports, such as micro- and mesoporous materials [1,36].

In the present work, a set of ceria-zirconia nanocatalysts, with different Zr-contents (in the range 10–30 at.%) and structural properties, has been prepared to study both the effect of Zr-loading and the surface-dependency activity towards CO oxidation, a probe reaction for more complex oxidation processes. Then, the physico-chemical features of the prepared materials have been investigated using complementary techniques.

## 2. Experimental

### 2.1. Preparation of the samples

A set of three nanostructured ceria-zirconia catalysts (denoted hereafter as  $\text{Ce}_x\text{Zr}_{1-x}\text{O}_2-\text{NP}$  where NP means nano-polyhedra, and  $x = 0.9, 0.8$  or  $0.7$  indicates the atomic ratio of Ce/Ce + Zr) were synthesized by hydrothermal procedure. Briefly, proper amounts of  $\text{Ce}(\text{NO}_3)_3 \cdot 6\text{H}_2\text{O}$  and  $\text{ZrOCl}_2 \cdot 8\text{H}_2\text{O}$  (Sigma-Aldrich) were dissolved in 30 mL of distilled water (“solution A”). Meanwhile, “solution B” was obtained by adding NaOH (24 g) to distilled water (35 mL). The two solutions were then mixed together and stirred at room temperature for 1 h to obtain a milky slurry. The latter was transferred to a Teflon autoclave (150 mL), which was 70% filled with deionized water, and then aged at 110 °C for 24 h. The fresh precipitate was separated by centrifugation, washed with deionized water and ethanol and dried at 90 °C overnight. Finally, the powder was calcined at 550 °C for 4 h.

An ordered mesoporous ceria-zirconia catalyst (denoted as  $\text{Ce}_{0.9}\text{Zr}_{0.1}\text{O}_2-\text{M}$ ) was prepared by nanocasting procedure using the KIT-6 silica-based template: 0.35 g of  $\text{Ce}(\text{NO}_3)_3 \cdot 6\text{H}_2\text{O}$  and 0.05 g of  $\text{ZrO}(\text{NO}_3)_2$  (Sigma-Aldrich) were dissolved in 5 mL of absolute ethanol. Then, 0.15 g of KIT-6 (ACS materials) was added to this

solution and heated at 60 °C under vigorous stirring for 30 min. When the ethanol had evaporated, the Ce-precursor/silica composite was calcined at 350 °C for 4 h. The impregnation step was repeated in order to achieve higher ceria-zirconia loadings. The powder was dried at 110 °C overnight and calcined at 550 °C for 6 h. The silica template was then removed and treated three times with a 2 M NaOH solution at 50 °C (10 min each time). Finally, the obtained powder was dried at 90 °C overnight.

$\text{Ce}_{0.9}\text{Zr}_{0.1}\text{O}_2-\text{NP}/\text{FAU}$  catalyst was prepared by impregnation of Faujasite-type zeolite (Sigma-Aldrich). The sample was obtained by adding proper amounts of  $\text{Ce}_{0.9}\text{Zr}_{0.1}\text{O}_2-\text{NP}$  and FAU zeolite in water ( $\text{Ce}_{0.9}\text{Zr}_{0.1}\text{O}_2-\text{NP}$  content = 50 wt.%), and placing the final mixture in a rotary evaporator at 60 °C to remove the water. The solid obtained was then dried at 90 °C overnight.

For comparison, a ceria-zirconia sample (denoted as  $\text{Ce}_{0.9}\text{Zr}_{0.1}\text{O}_2-\text{SCS}$ ) was prepared by solution combustion synthesis (SCS) [38]. In short, a solution of  $\text{Ce}(\text{NO}_3)_3 \cdot 6\text{H}_2\text{O}$  (1.9 g),  $\text{ZrO}(\text{NO}_3)_2$  (0.11 g) and urea (0.8 g) was placed in an oven at 600 °C for 20 min. The resultant powder was washed with deionized water and then dried at 90 °C overnight.

### 2.2. Characterization of the catalysts

The powder X-ray diffraction (XRD) patterns were collected on a X'Pert Philips PW3040 diffractometer using  $\text{Cu K}\alpha$  radiation ( $2\theta$  range = 20°–90°; step = 0.05°  $2\theta$ ; time per step = 0.2 s). The diffraction peaks were indexed according to the Powder Data File database (PDF 2000, International Centre of Diffraction Data, Pennsylvania).

The textural properties, i.e. specific surface area ( $S_{\text{BET}}$ ), total pore volume ( $V_p$ ) and pore diameter ( $D_p$ ), were obtained by  $\text{N}_2$  sorption at –196 °C (Micrometrics ASAP 2020) on samples previously outgassed at 200 °C for 4 h. The specific surface area of the samples was calculated using the BET method, whereas the pore diameter was evaluated by applying the Barrett-Joyner-Halenda (BJH) algorithm to the isotherm desorption branch.

Sample morphology was studied by using a field emission scanning electron microscope (FESEM Zeiss MERLIN, Gemini-II column) and a transmission electron microscope (TEM, Jeol JEM 3010 operating at 200 kV). The Ce/Zr-content in the samples was determined through EDS analysis (Oxford X-ACT): 5 different spots with a 10–50 nm diameter were selected in representative zones of the sample, and the average Ce/Zr-content was then calculated.

Raman spectra were recorded on a micro-Raman system (Renishaw ViaReflex) equipped with an Ar-Kr laser, by exciting at 514.5 nm.

X-ray photoelectron spectroscopy (XPS) measurements were carried out on PHI 5000 Versa probe apparatus using a band-pass energy of 187.85 eV, a 45° take off angle and a 100.0  $\mu\text{m}$  diameter X-ray spot size. Curve-fits were performed by means of Multipack 9.0 software.

IR spectra were collected on an FT-IR spectrophotometer (Equinox 55, Bruker), equipped with an MCT (Mercury Cadmium Telluride) cryodetector. To remove water and other atmospheric contaminants, wafers were pre-outgassed at either 150 or 450 °C for 1 h before adsorption of probe molecules. Pre-treatments were carried out using a standard vacuum frame in an IR quartz cell equipped with KBr windows.

IR spectra concerning CO adsorption were recorded at the nominal boiling point of nitrogen (–196 °C), by dosing increasing amounts of carbon monoxide (0.05–20.0 mbar equilibrium pressure) on samples previously outgassed inside a home-made quartz IR cell, allowing both dosing of gases and addition of a coolant. After each measurement, an evacuation step was performed at room temperature to check the reversibility of the interaction.

### 2.3. Catalytic activity tests

The activity of the catalysts was evaluated by temperature programmed oxidation (TPO), according to standard operating procedures [39]: a gas mixture (1000 ppm CO; 10 vol.% O<sub>2</sub>, He = balance) was fed, via a set of mass flow controllers, into the catalytic fixed-bed micro-reactor enclosed in a quartz tube placed in an electric oven (W/F = 0.12 g s<sup>-1</sup> cm<sup>-3</sup>). The tubular quartz micro-reactor (4 mm i.d.) was loaded with 0.1 g of pelletized catalyst (0.2–0.5 mm granules). The reaction temperature was controlled through a PID-regulated oven and varied from room temperature up to 450 °C at a 5 °C min<sup>-1</sup> rate. The temperature was measured by means of a thermocouple placed close to the catalytic bed. The CO conversion was monitored with a CO/CO<sub>2</sub> NDIR analyser (ABB). A computer recorded both the fixed bed temperature and the CO/CO<sub>2</sub> outlet concentration as a function of time. Temperatures corresponding to 10%, 50% and 90% CO conversion (denoted as T<sub>10%</sub>, T<sub>50%</sub>, T<sub>90%</sub>, respectively) were taken as indices of the catalytic activity.

## 3. Results and discussion

### 3.1. Textural features of the samples

A summary of the main textural and structural properties of the prepared catalysts is reported in Table 1. Detailed data have been reported elsewhere [8]. Fig. S1 (Supporting information) shows the wide-angle XRD patterns of the ceria-zirconia samples: the observed diffraction peaks can all be indexed as cubic fluorite-type structure (*Fm3m* symmetry), corresponding to the (111), (200), (220), (311), (222), (400), (331) and (420) planes [40,41]. No extra-peaks are detected, thus showing the presence of a single ceria-zirconia phase for all the samples. The XRD peaks of the Faujasite-type support (peaks denoted with “o”) are also present with the Ce<sub>0.9</sub>Zr<sub>0.1</sub>O<sub>2</sub>–NP/FAU catalyst. The low-angle XRD diffractogram of the Ce<sub>0.9</sub>Zr<sub>0.1</sub>O<sub>2</sub>–M (Fig. S2, Supporting Information), confirms that the replication of the KIT-6 template was preserved [37].

The relative amount of the (110), (100) and (111) planes have been estimated by means of the XRD peak intensity ratios. As shown in Table 1, the highest (220)/(111) and (200)/(111) values were obtained for the Ce<sub>0.9</sub>Zr<sub>0.1</sub>O<sub>2</sub>–NP (and then for the Ce<sub>0.9</sub>Zr<sub>0.1</sub>O<sub>2</sub>–NP/FAU), thus showing the richest population of highly reactive (100) and (110) exposed planes. On the other hand, the Ce<sub>0.9</sub>Zr<sub>0.1</sub>O<sub>2</sub>–SCS exhibits the highest amount of (111) surfaces.

Fig. S3 (Supporting information) reports N<sub>2</sub> isotherms at -196 °C: the Ce<sub>0.9</sub>Zr<sub>0.1</sub>O<sub>2</sub>–M catalyst shows IV-type isotherms, which is typical for mesoporous materials, with hysteresis loops closing at about 0.85 P/P<sup>0</sup>, whereas the Ce<sub>0.9</sub>Zr<sub>0.1</sub>O<sub>2</sub>/FAU exhibits type I isotherms, with a very steep uptake at low relative pressures (due to micropore filling), followed by a plateau to near saturation pressure. The latter catalyst exhibits good textural features (S<sub>BET</sub> = 521 m<sup>2</sup> g<sup>-1</sup> and V<sub>p</sub> = 0.25 cm<sup>3</sup> g<sup>-1</sup>) because of the high surface-area of the FAU-type zeolite. As known, the Faujasite framework consists of sodalite cages connected through hexagonal prisms. The cavities are perpendicular to each other in a three-dimensional (3-D) system. Each cavity, which is formed by a 12-membered ring, has a relatively large diameter of 7.4 Å. The inner cavity has a diameter of 12 Å and is surrounded by 10 sodalite cages [42]. Thus, the FAU-type support might promote the overall catalytic activity, allowing a high dispersion of the nanoparticles on the external surface. Moreover, longer residence times of molecules (reactants and products) in the 3-D cavities should appear, thus favouring total oxidation reactions [43]. On the other hand, lower adsorption capacities are expected for the Ce<sub>0.9</sub>Zr<sub>0.1</sub>O<sub>2</sub>–SCS sample, as reflected by the N<sub>2</sub> sorption isotherms. Noteworthy, different

textural properties appear for the Ce<sub>x</sub>Zr<sub>1-x</sub>O<sub>2</sub>–NP (S<sub>BET</sub> = 2–3 m<sup>2</sup> g<sup>-1</sup> and V<sub>p</sub> = 0.01 cm<sup>3</sup> g<sup>-1</sup>).

The morphological features of the prepared catalysts were observed by electron microscopy. FESEM images of the Ce<sub>0.9</sub>Zr<sub>0.1</sub>O<sub>2</sub>–NP, Ce<sub>0.8</sub>Zr<sub>0.2</sub>O<sub>2</sub>–NP and Ce<sub>0.7</sub>Zr<sub>0.3</sub>O<sub>2</sub>–NP samples (Fig. 1a–c, respectively) show the presence of particle aggregates in the size range of 20–80 nm. Fig. 1d reveals a fairly high dispersion of the Ce<sub>0.9</sub>Zr<sub>0.1</sub>O<sub>2</sub>–NP on the FAU surface, thus suggesting that both CO and O<sub>2</sub> molecules can easily reach the reactive planes, while the Ce<sub>0.9</sub>Zr<sub>0.1</sub>O<sub>2</sub>–SCS exhibits a self-assembly of particles, thus leading to interparticle voids. The periodic ordered channels of the Ce<sub>0.9</sub>Zr<sub>0.1</sub>O<sub>2</sub>–M sample are shown in Fig. 1e, in agreement with the low-angle XRD pattern (*vide supra*).

TEM images of the ceria-zirconia nanocatalysts are shown in Fig. 2. A careful morphological analysis of the Ce<sub>x</sub>Zr<sub>1-x</sub>O<sub>2</sub>–NP sample reveals the presence of nano-polyhedra (i.e. truncated octahedral and octahedral shapes) with sizes of about 20–40 nm.

The latter exhibit convex shapes with the Euler characteristic of the sphere (X=2) and are dominated by different crystallographic faces, thus reflecting various surface atom densities, electronic structures, bonds, chemical reactivities and thermodynamic properties. The equilibrium shape of these nanostructures is determined by the Wulff rule [44], according to which the convex envelope of planes (perpendicular to the surface normal) minimizes the surface energy for a given enclosed volume (Scheme 1). However, the Wulff construction minimizes only the surface energy of a particular atomic packing and not the total energy of the particle [24]. Thus, non-convex structures (X ≠ 2), like Kepler-Poinsot polyhedra, might also appear in ceria and related materials, as a consequence of selective passivation and blocking of edge and corner sites during growth, coupled with anisotropic growth rates, although they have not been observed in this set of ceria-zirconia catalysts. Fig. 2a shows the TEM image of the Ce<sub>0.9</sub>Zr<sub>0.1</sub>O<sub>2</sub>–NP sample with (100)-type planes at 90°, as revealed by the Fourier Transform image. The (110) planes that originate from the truncation of the particle edges can also be seen at 45°. Similar polyhedra would be observed for both Ce<sub>0.8</sub>Zr<sub>0.2</sub>O<sub>2</sub>–NP and Ce<sub>0.7</sub>Zr<sub>0.3</sub>O<sub>2</sub>–NP (Fig. 2b and c, respectively). The micrograph of the Ce<sub>0.9</sub>Zr<sub>0.1</sub>O<sub>2</sub>–NP/FAU (Fig. 2d) confirms the high dispersion of the active phase (Ce<sub>0.9</sub>Zr<sub>0.1</sub>O<sub>2</sub>–NP) over the FAU surface. Finally, images of the Ce<sub>0.9</sub>Zr<sub>0.1</sub>O<sub>2</sub>–M sample are shown in Fig. 2e and f: well-ordered arrays of mesostructured channels appear, in agreement with the XRD analysis. The particles are highly crystalline and display an interplanar spacing of ca. 0.30 nm, corresponding to the (111) lattice planes. The pore wall thickness estimated from the TEM investigation was about 8 nm, which is slightly more than 6 nm, calculated with the BET method. The TEM images of Ce<sub>0.9</sub>Zr<sub>0.1</sub>O<sub>2</sub>–SCS (not reported for the sake of brevity) revealed the presence of particles in the 16–20 nm size range.

### 3.2. The Nature of Ce and Zr species as studied by X-ray photoelectron and Raman spectroscopies

The reduction behaviour of the these Ce-Zr-O materials has been described elsewhere [8]. In short, it has been shown that the presence of non-reducible Zr<sup>4+</sup> ions in the CeO<sub>2</sub> lattice, as well as the structural and electronic parameters, may affect the redox properties and then the capacity of ceria-zirconia catalysts to release oxygen under reducing conditions. Indeed, H<sub>2</sub>-TPR profiles of ceria-zirconia materials are more complex than those of pure ceria, since a number of parameters (e.g. Zr/Ce ratios, structural defects, changes in the electronic structure, etc.) may affect to the reducibility of the catalytic materials. In particular, a higher mobility of lattice oxygen has been observed within the Ce<sub>x</sub>Zr<sub>1-x</sub>O<sub>2</sub>–NP

**Table 1**

Textural properties of the samples, as derived from both N<sub>2</sub> isotherms at –196 °C and XRD analysis.

Sample	S <sub>BET</sub> <sup>a</sup> (m <sup>2</sup> g <sup>-1</sup> )	V <sub>p</sub> <sup>b</sup> (cm <sup>3</sup> g <sup>-1</sup> )	D <sub>p</sub> <sup>c</sup> (nm)	Intensity ratios <sup>d</sup>	
				(200)/(111)	(220)/(111)
Ce <sub>0.9</sub> Zr <sub>0.1</sub> O <sub>2</sub> —NP	2	0.01	—	0.39	0.61
Ce <sub>0.8</sub> Zr <sub>0.2</sub> O <sub>2</sub> —NP	2	0.01	—	0.36	0.54
Ce <sub>0.7</sub> Zr <sub>0.3</sub> O <sub>2</sub> —NP	4	0.01	—	0.33	0.47
Ce <sub>0.9</sub> Zr <sub>0.1</sub> O <sub>2</sub> —M	121	0.24	6	0.36	0.52
Ce <sub>0.9</sub> Zr <sub>0.1</sub> O <sub>2</sub> —SCS	20	0.03	6	0.28	0.46
Ce <sub>0.9</sub> Zr <sub>0.1</sub> O <sub>2</sub> —NP/FAU	521	0.25	0.5	0.39	0.61

<sup>a</sup> S<sub>BET</sub> = specific surface area.

<sup>b</sup> V<sub>p</sub> = total pore volume.

<sup>c</sup> D<sub>p</sub> = pore diameter calculated according to the BJH method.

<sup>d</sup> XRD peak intensity ratios.

**Table 2**

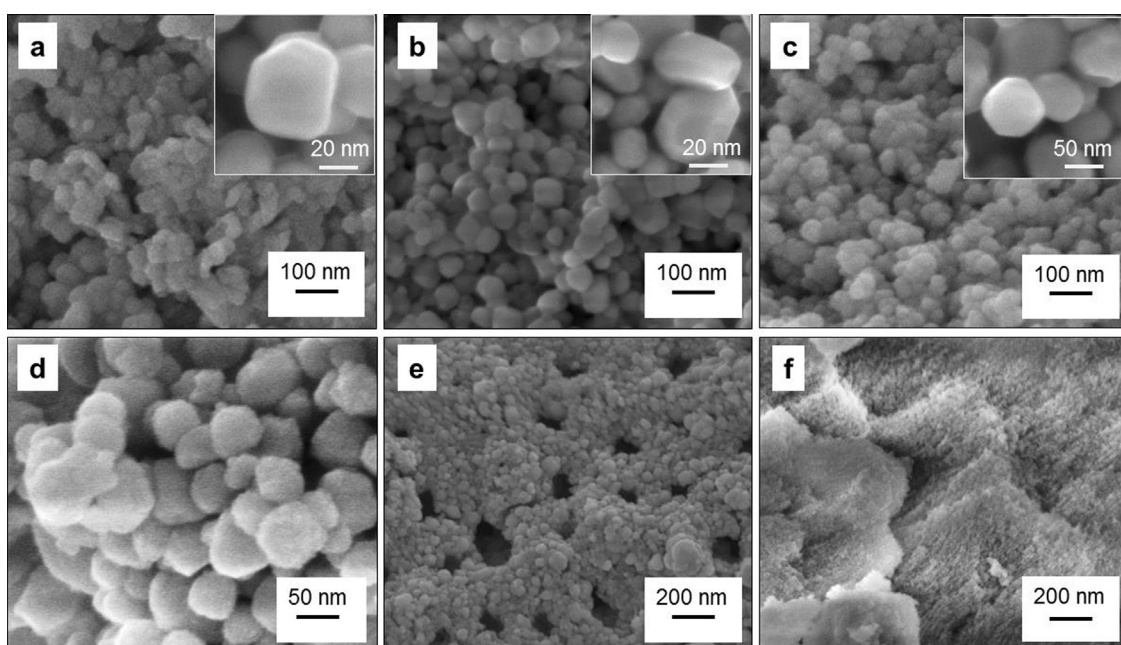
XPS results of curve-fittings on the O 1s and Ce 3d binding energy of samples.

Sample	$\frac{O_\alpha}{O_\beta}$	Ce <sup>3+</sup> ( $v_1 + u_1$ ) (%)
Ce <sub>0.9</sub> Zr <sub>0.1</sub> O <sub>2</sub> —NP	0.10	13.9
Ce <sub>0.8</sub> Zr <sub>0.2</sub> O <sub>2</sub> —NP	0.12	11.1
Ce <sub>0.7</sub> Zr <sub>0.3</sub> O <sub>2</sub> —NP	0.13	10.5
Ce <sub>0.9</sub> Zr <sub>0.1</sub> O <sub>2</sub> —NP/FAU	0.57	8.3
Ce <sub>0.9</sub> Zr <sub>0.1</sub> O <sub>2</sub> —M	0.52	12.6
Ce <sub>0.9</sub> Zr <sub>0.1</sub> O <sub>2</sub> —SCS	0.50	19.7

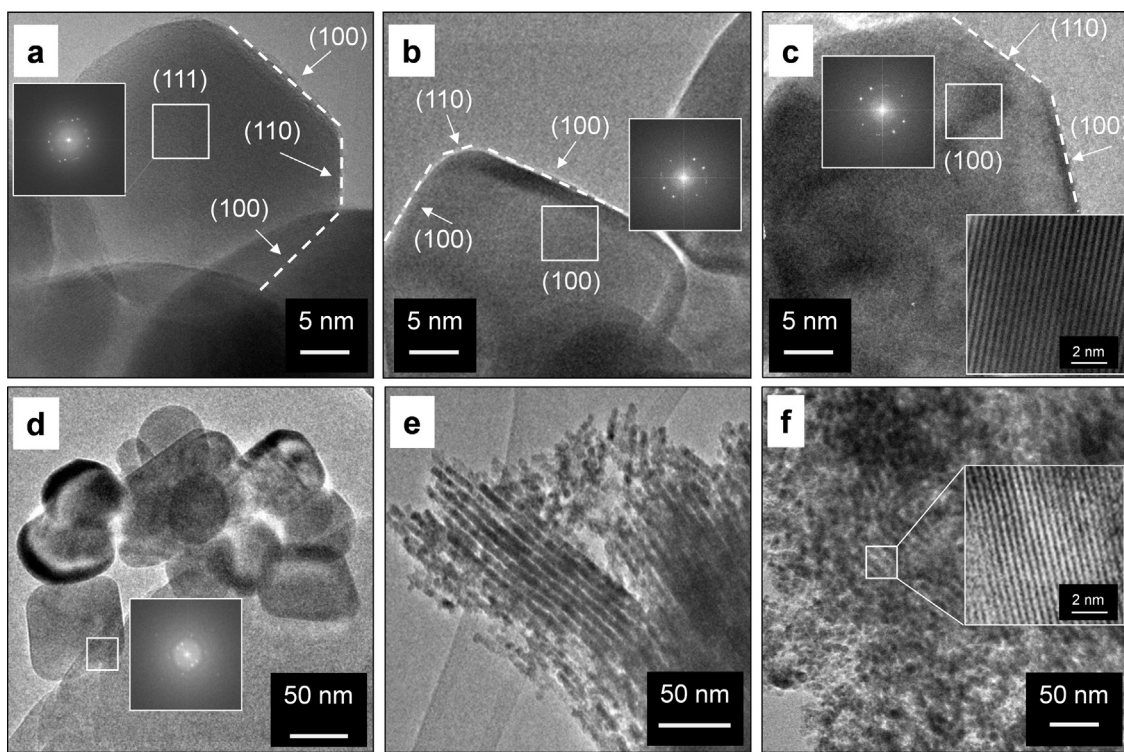
catalysts (especially in the Ce<sub>0.9</sub>Zr<sub>0.1</sub>O<sub>2</sub>—NP), as well as an easier reducibility compared to high-surface area catalysts.

Fig. S4 (Supporting information) shows the XPS spectra in the O 1s, Ce and Zr 3d BE ranges. The O 1s spectra reports two peaks, which are due to either chemisorbed oxygen (O<sub>α</sub> species) or lattice oxygen (O<sub>β</sub> species). The signal at 528.6–528.9 eV corresponds to O<sub>β</sub> (i.e. O<sup>2-</sup>), whereas the peak at 529.9–531.4 eV can be ascribed to surface oxygens (i.e. O<sub>2</sub><sup>2-</sup>, O<sup>-</sup>, OH<sup>-</sup>, CO<sub>3</sub><sup>2-</sup>) [45–47]. With the Ce<sub>0.9</sub>Zr<sub>0.1</sub>O<sub>2</sub>—NP, the signal related to the O<sub>β</sub> species appears at a slightly higher BE (528.9 eV), thus revealing a lower nucleophilicity of the lattice oxygen ions. As expected, a richer population of O<sub>α</sub> species was obtained for high-surface area materials than for Ce<sub>x</sub>Zr<sub>1-x</sub>O<sub>2</sub>—NP, because of the richer population of surface hydroxyls, carbonates and adsorbed oxygen (Table 2). On the other hand,

the Ce<sub>x</sub>Zr<sub>1-x</sub>O<sub>2</sub>—NP mainly display O<sub>β</sub> species, which play a key role in the CO oxidation over ceria-based catalysts (kinetically modelled via a MVK-type mechanism) [1,13,16,17,29]. The Ce 3d core-level spectra shows signals related to Ce<sup>3+</sup> and Ce<sup>4+</sup> ions, where the “v” and “u” peaks correspond to the 3d<sub>5/2</sub> and 3d<sub>3/2</sub> states, respectively (Table S1, Supporting information). The doublets (v<sub>0</sub>, u<sub>0</sub>), (v<sub>2</sub>, u<sub>2</sub>), and (v<sub>3</sub>, u<sub>3</sub>) are assigned to the different states of Ce<sup>4+</sup>, whereas the doublet (v<sub>1</sub>, u<sub>1</sub>) is due to the Ce<sup>3+</sup> species [47]. Table 2 summarizes the relative abundance of the Ce<sup>3+</sup> species (at.%) for each catalyst kept under partial reducing conditions (ultra-high vacuum and electron beam irradiation) estimated considering the deconvolution results of Ce 3d. With Ce<sub>x</sub>Zr<sub>1-x</sub>O<sub>2</sub>—NP catalysts, the relative amount of Ce<sup>3+</sup> ions decreases with an increase in the Zr-content, thus showing the role of Zr<sup>4+</sup> ions in retaining a higher oxidation state of the Ce species [48]. The Ce<sup>3+</sup> content of Ce<sub>0.9</sub>Zr<sub>0.1</sub>O<sub>2</sub>—SCS (namely, 19.7 at.%) is higher than that of the other samples, because of the higher thermal treatment used during the SCS procedure (600 °C) [49]. The Zr 3d spectra in the 181.9–182.3 eV range denote the Zr 3d<sub>5/2</sub> states, whereas the signals at 184.4 eV correspond to the Zr 3d<sub>3/2</sub> levels. According to the BE of Zr 3d<sub>5/2</sub>, Ce-Zr mixed oxide can be well distinguished from the ZrO<sub>2</sub> phase (182.9 eV [50,51]). No signal due to the ZrO<sub>2</sub> phase can be detected for any of the prepared catalysts. As expected, the Zr 3d peak intensity increases as the Zr-content rises from 10 to 30 at.%, however no significant shift to a higher BE appears for the Ce<sub>x</sub>Zr<sub>1-x</sub>O<sub>2</sub>—NP catalysts. This means



**Fig. 1.** FESEM images of (a) Ce<sub>0.9</sub>Zr<sub>0.1</sub>O<sub>2</sub>—NP, (b) Ce<sub>0.8</sub>Zr<sub>0.2</sub>O<sub>2</sub>—NP, (c) Ce<sub>0.7</sub>Zr<sub>0.3</sub>O<sub>2</sub>—NP, (d) Ce<sub>0.9</sub>Zr<sub>0.1</sub>O<sub>2</sub>—NP/FAU, (e) Ce<sub>0.9</sub>Zr<sub>0.1</sub>O<sub>2</sub>—SCS and (f) Ce<sub>0.9</sub>Zr<sub>0.1</sub>O<sub>2</sub>—M samples.



**Fig. 2.** TEM images of the (a)  $\text{Ce}_{0.9}\text{Zr}_{0.1}\text{O}_2$ —NP, (b)  $\text{Ce}_{0.8}\text{Zr}_{0.2}\text{O}_2$ —NP, (c)  $\text{Ce}_{0.7}\text{Zr}_{0.3}\text{O}_2$ —NP, (d)  $\text{Ce}_{0.9}\text{Zr}_{0.1}\text{O}_2$ —NP/FAU and (e and f)  $\text{Ce}_{0.9}\text{Zr}_{0.1}\text{O}_2$ —M samples.

that  $\text{Zr}^{4+}$  ions are well dispersed and incorporated into the solid framework.

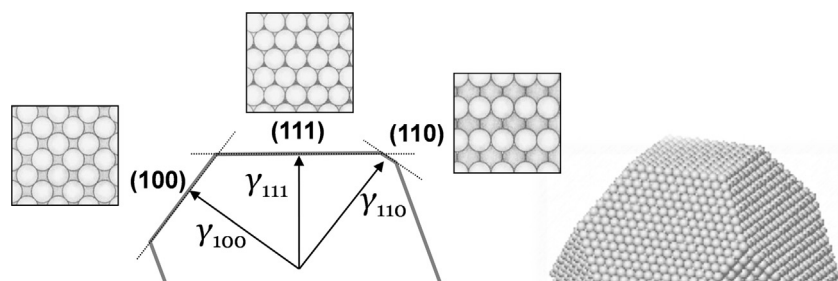
Raman spectroscopy allows us to probe the presence of oxygen defects in ceria-based materials. The relative intensity ratio between the defect band ( $I_D$ ) and the  $F_{2g}$  band ( $I_{F2g}$ ) of the fluorite phase can be used as an indicator of the  $\text{O}_v$  density [52]. The Raman spectra of the ceria-zirconia catalysts are reported in Fig. 3. As a whole, all samples exhibit the signals corresponding to the symmetric breathing mode ( $F_{2g}$ ) of oxygen atoms around  $\text{Ce}^{4+}$  ions at ca.  $460\text{ cm}^{-1}$  (characteristic peak of the fluorite structure) and a low-intensity band at ca.  $600\text{ cm}^{-1}$  attributed to the presence of Frenkel-type anion defects in the ceria lattice [53–56]. In the latter case, an oxygen ion is displaced from its lattice position to an interstitial position, thus leading to a vacancy at its initial position and a defect at the interstitial site. The ratio between the areas of the  $\text{O}_v$  and  $F_{2g}$  peaks is the most appropriate way to compare the population of oxygen vacancies in different solids: the higher the  $\text{O}_v/F_{2g}$  area ratio value the higher the amount of oxygen vacancies [53–55]. In the present case, the  $\text{O}_v/F_{2g}$  values obtained for the prepared catalysts confirm that nano-polyhedra (especially, the  $\text{Ce}_{0.9}\text{Zr}_{0.1}\text{O}_2$ —NP sample) have higher  $\text{O}_v$  than porous catalysts with the same Zr-content (namely, 10 at.%). The addition of  $\text{Zr}^{4+}$  ions favours the formation of additional vacancies in

the nano-polyhedra, especially with Zr 30 at.%. On the other hand, the  $F_{2g}$  signal of  $\text{CeO}_2$  is blue-shifted by  $11\text{ cm}^{-1}$  in the case of  $\text{Ce}_{0.7}\text{Zr}_{0.3}$ —NP, possibly due to the higher amount of  $\text{Ce}^{4+}$  species, in fair agreement with the XPS analysis (*vide supra*, [8]).

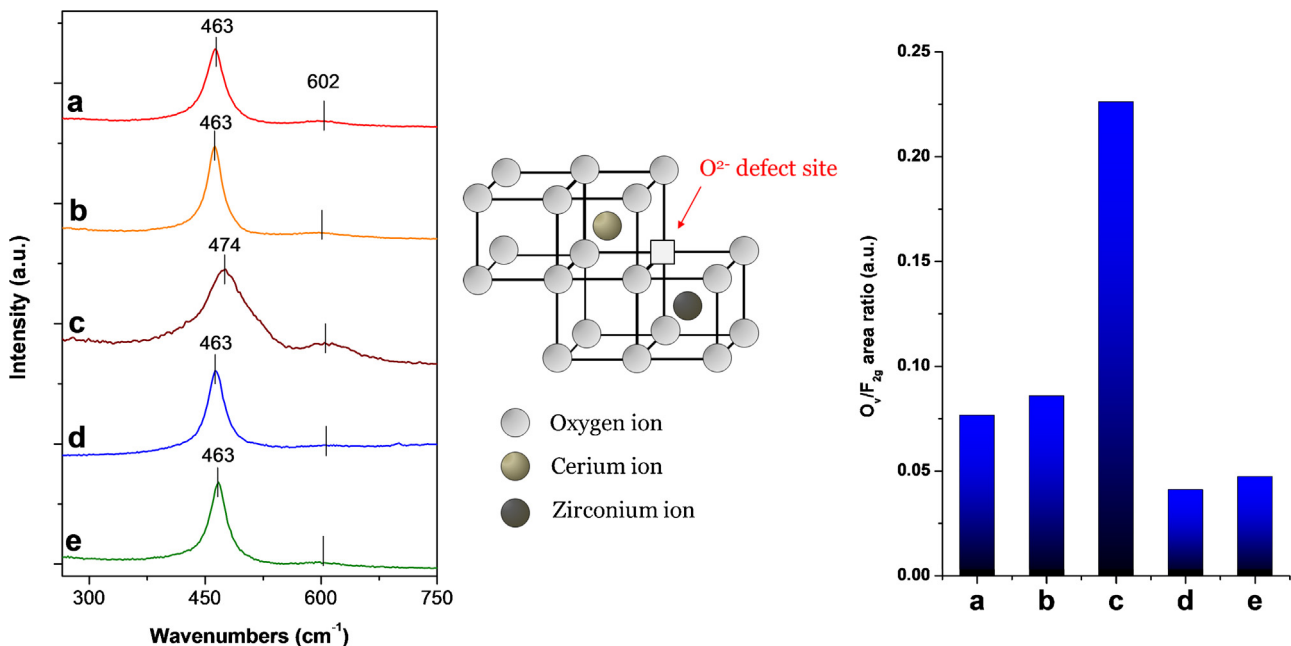
### 3.3. FT-IR study of surface properties

Fig. 4 shows the FT-IR spectra of the samples outgassed at  $150$  and  $450^\circ\text{C}$  before dosing CO. All the reported spectra were normalized to unit specific weight to allow a comparison to be made. As a whole, the IR spectra of samples show three distinct regions, corresponding to hydroxyl, formate and carbonate species.

In the O–H stretching region ( $3800$ – $3000\text{ cm}^{-1}$ ) the following bands can be distinguished for the prepared catalysts: isolated hydroxyls ( $3710$ – $3700\text{ cm}^{-1}$ ), bridging hydroxyls ( $3660$ – $3640\text{ cm}^{-1}$ ), multiple bonded hydroxyls ( $3550$ – $3500\text{ cm}^{-1}$ ) and hydrogen bridging hydroxyls (broad band at  $3400$ – $3100\text{ cm}^{-1}$ ) [56,57]. The catalysts outgassed at  $150^\circ\text{C}$  (Fig. 4A) show similar O–H stretching bands, although with different intensities: both  $\text{Ce}_{0.9}\text{Zr}_{0.1}$ —NP and  $\text{Ce}_{0.8}\text{Zr}_{0.2}$ —NP exhibit higher amounts of bridged hydroxyls ( $3655\text{ cm}^{-1}$ ) and multiple bonded OH groups ( $3510\text{ cm}^{-1}$ ), in agreement with the presence of more accessible and reactive planes [57]. However, at higher Zr-content (namely,



**Scheme 1.** Cross section of a small particle based on the Wulff construction using surface energies ( $\gamma$ ) for the (111), (110) and (100) planes.



**Fig. 3.** Micro-Raman spectra, in the 265–750 cm<sup>-1</sup> range, recorded at ambient conditions with the (a) Ce<sub>0.9</sub>Zr<sub>0.1</sub>O<sub>2</sub>—NP, (b) Ce<sub>0.8</sub>Zr<sub>0.2</sub>O<sub>2</sub>—NP, (c) Ce<sub>0.7</sub>Zr<sub>0.3</sub>O<sub>2</sub>—NP, (d) Ce<sub>0.9</sub>Zr<sub>0.1</sub>O<sub>2</sub>—M and (e) Ce<sub>0.9</sub>Zr<sub>0.1</sub>O<sub>2</sub>—SCS samples (left). O<sub>v</sub>/F<sub>2g</sub> area ratios of the same catalysts (right). In the middle: schematic representation of oxygen vacancy at the surface of Ce-Zr mixed oxide.

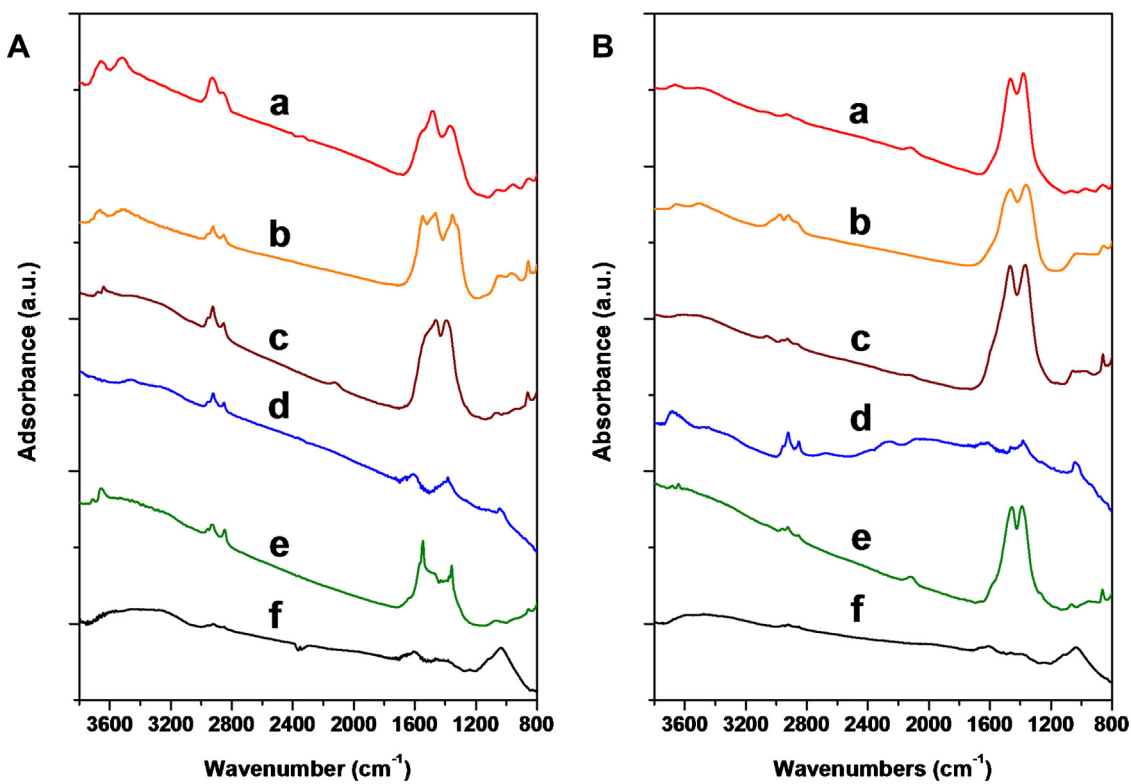
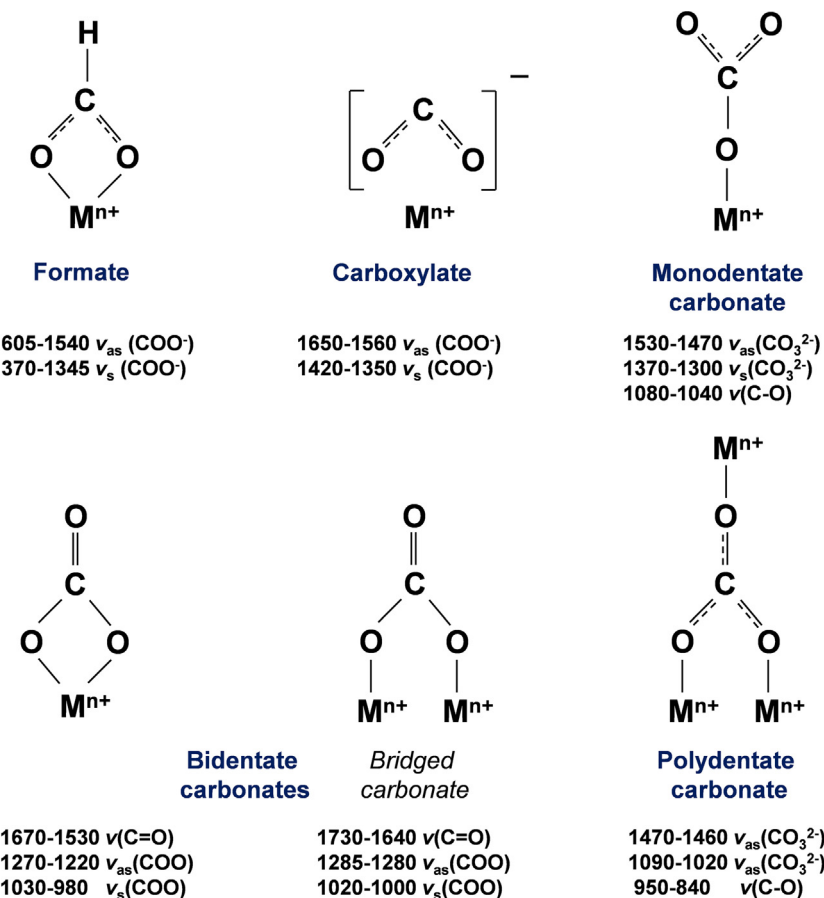


**Fig. 4.** FT-IR spectra of the (a) Ce<sub>0.9</sub>Zr<sub>0.1</sub>O<sub>2</sub>—NP, (b) Ce<sub>0.8</sub>Zr<sub>0.2</sub>O<sub>2</sub>—NP, (c) Ce<sub>0.7</sub>Zr<sub>0.3</sub>O<sub>2</sub>—NP, (d) Ce<sub>0.9</sub>Zr<sub>0.1</sub>O<sub>2</sub>—M, (e) Ce<sub>0.9</sub>Zr<sub>0.1</sub>O<sub>2</sub>—SCS and (f) Ce<sub>0.9</sub>Zr<sub>0.1</sub>O<sub>2</sub>—NP/FAU samples outgassed at 150 °C (Section A) and 450 °C (Section B).

Ce<sub>0.7</sub>Zr<sub>0.3</sub>O<sub>2</sub>—NP) it is possible to observe a richer population of hydrogen bridging OH adsorbed either on Zr or Ce cations [57,58]. Different IR profiles appear for the high-surface area samples: (i) the Ce<sub>0.9</sub>Zr<sub>0.1</sub>O<sub>2</sub>—SCS reveals signals due to isolated (3713 cm<sup>-1</sup>) and bridging OH groups (3653 cm<sup>-1</sup>); (ii) the Ce<sub>0.9</sub>Zr<sub>0.1</sub>O<sub>2</sub>—M shows only few hydrogen bridging OH exposed at the surface, likely due to the easier removal of water in the mesoporous network [59]; (iii) the

high amount of H-bonded hydroxyls on the Ce<sub>0.9</sub>Zr<sub>0.1</sub>O<sub>2</sub>—NP/FAU, and the low active phase content (namely, 50 wt.% of Ce-Zr mixed oxide), superimposes the OH stretching modes on the active planes of Ce<sub>0.9</sub>Zr<sub>0.1</sub>O<sub>2</sub>—NP.

At lower wavenumbers, all spectra show signals at 2930 and 2845 cm<sup>-1</sup> corresponding to C—H stretching vibrations of formate species (Scheme 2) [56]. The latter bands have similar intensities



**Scheme 2.** Types and FTIR peak assignments of formate and carbonate-carboxylate species observed on ceria-zirconia catalysts.

for all the prepared samples, except for the Ce<sub>0.9</sub>Zr<sub>0.1</sub>O<sub>2</sub>—NP/FAU, thus confirming that formates are chemisorbed on the Ce-Zr mixed oxide. Finally, the signals in the 1800–1000 cm<sup>-1</sup> range can be readily assigned to C–O stretching and bending modes of carbonate and formate species. When acting as an electrophile, CO<sub>2</sub> reacts with oxygen defects or hydroxide species giving rise to formates (1558 cm<sup>-1</sup>), energetically stable bi- and polidentate carbonates [32], which are particularly abundant on the Ce<sub>x</sub>–Zr<sub>1-x</sub>O<sub>2</sub>—NP samples (bands at 1485, 1363, 1056 and 854 cm<sup>-1</sup>) [56,60,61]; see Scheme 2 for the structures and peak assignments.

On the other hand, only few carbonate-carboxylate compounds appear on the Ce<sub>0.9</sub>Zr<sub>0.1</sub>O<sub>2</sub>—M surface (peaks at 1609, 1376 and 1036 cm<sup>-1</sup>), despite its higher surface area. Similarly, an abundant population of formates (signal at 1546 cm<sup>-1</sup>) but few carbonates can be observed on the Ce<sub>0.9</sub>Zr<sub>0.1</sub>O<sub>2</sub>—SCS sample. IR spectra of the samples outgassed at 300 °C show comparable profiles and peak intensities (spectra not reported for the sake of brevity), thus revealing the good thermal stability of carbonate/formate species obtained by interaction of lattice oxygen/hydroxyl species with atmospheric CO<sub>2</sub>. Polydentate carbonates are still present on the samples outgassed at 450 °C (Fig. 4B), whereas the formate species (peaks at 2945, 2840 and 1546 cm<sup>-1</sup>) disappeared, thus reflecting their lower stability, in fair agreement with previous studies [56]. Moreover, the bands in the O–H stretching region decreased for all the samples, as a consequence of the surface dehydroxylation.

### 3.4. FT-IR analysis by means of CO adsorption at nominal –196 °C

Carbon monoxide is widely used as a probe molecule to detect the presence and the nature of the Lewis acidity, as well as the

Brønsted acidic sites to which it may H-bond. As a whole, when the interaction between CO and the cationic site basically has an electrostatic nature (as in previously mentioned cases), a hypsochromic shift occurs with respect to the free CO molecule (2143 cm<sup>-1</sup>). However, there are many factors affecting the vibrational frequency of CO after adsorption: the electrostatic,  $\sigma$  and  $\pi$  contributions to the bonding of CO in M<sup>n+</sup>-CO species are the most important factors for the shift of CO frequency. Both the electrostatic interaction and the  $\sigma$  bond cause positive (hypsochromic) shifts, whereas the  $\pi$  bond causes negative (bathochromic) frequency shifts. The bathochromic shift caused by the  $\pi$ -back donation competes with the positive shift induced by the other two bonding mechanisms. Specifically, the strength of the  $\pi$  contribution increases with decreasing positive charge of the metal ion, and so a stronger  $\pi$  back-donation is expected for Ce<sup>3+</sup> instead of Ce<sup>4+</sup> [62]. To better evaluate the nature of active sites and avoid surface carbonation, CO adsorption was studied at the temperature of liquid nitrogen [59,61–63].

Figs. 5 and 6 show difference spectra in the CO stretch range of two representative samples, namely the Ce<sub>0.9</sub>Zr<sub>0.1</sub>O<sub>2</sub>—NP and Ce<sub>0.9</sub>Zr<sub>0.1</sub>O<sub>2</sub>—SCS outgassed at 150 °C (Section A) and 450 °C (Section B) obtained after subtracting those of the bare samples depicted in Fig. 4. The insets show the same difference spectra, in the hydroxyls stretch region, recorded after dosing ca. 20 mbar CO. CO adsorption on the Ce<sub>0.9</sub>Zr<sub>0.1</sub>O<sub>2</sub>—NP sample outgassed at 150 °C (Fig. 5A) gave rise to a band at 2159 cm<sup>-1</sup>, then shifted to 2152 cm<sup>-1</sup> ( $\Delta\nu = 7$  cm<sup>-1</sup>), due to physisorbed CO interacting with the solid surface through van der Waals forces and CO interactions with hydroxyl groups (Brønsted acidic sites) [63]. The weak signals at 2172 and 2130 cm<sup>-1</sup> can be attributed to CO bonded to un-

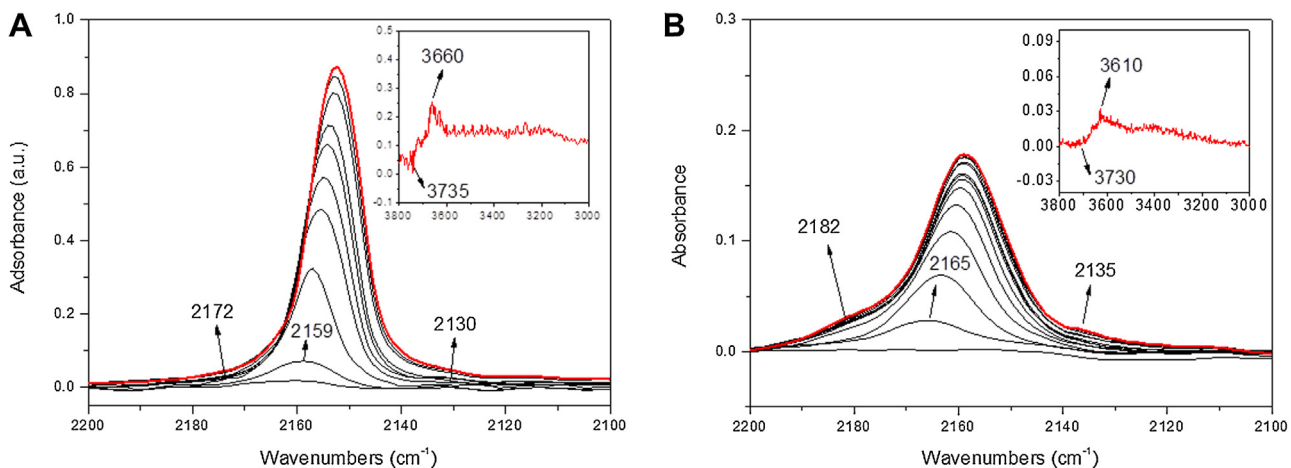


**Fig. 5.** FT-IR difference spectra, recorded after dosing CO (equilibrium pressure in the 0.01–20 mbar range) at nominal  $-196\text{ }^{\circ}\text{C}$  on  $\text{Ce}_{0.9}\text{Zr}_{0.1}\text{O}_2$ –NP sample outgassed at  $150\text{ }^{\circ}\text{C}$  (Section A) and  $450\text{ }^{\circ}\text{C}$  (Section B). Insets: same difference spectra in the OH stretching region (after dosing 20 mbar).

coordinated  $\text{Ce}^{4+}$  and  $\text{Ce}^{3+}$  ions [64], respectively, acting as Lewis acidic centres. Correspondingly, in the hydroxyls stretch region (inset), a weak negative band appears at  $3735\text{ cm}^{-1}$  due to the formation of  $\text{Ce}-\text{O H-CO}$  complexes (signal at ca.  $3660\text{ cm}^{-1}$ ) [65].

When the sample was outgassed at  $450\text{ }^{\circ}\text{C}$  (Fig. 5B), a weaker band occurred at  $2165\text{ cm}^{-1}$  (CO adsorbed on hydroxyl groups) and, correspondingly, a higher amount of coordinatively unsaturated  $\text{Ce}^{4+}$  and  $\text{Ce}^{3+}$  sites appeared at  $2182$  and  $2135\text{ cm}^{-1}$  [64], respectively (stronger Lewis acidic sites), as result of the surface de-hydroxylation. At the same time, in the OH stretch region, the intensity of signals decreased. Conversely, CO dosage on the  $\text{Ce}_{0.9}\text{Zr}_{0.1}\text{O}_2$ -SCS sample outgassed at  $150\text{ }^{\circ}\text{C}$  (Fig. 6A) brings about the following features: an intense peak at  $2157\text{ cm}^{-1}$  (physisorbed CO interacting with OH groups) and a weak signal at  $2174\text{ cm}^{-1}$  ( $\text{Ce}^{4+}$  cations). Signals corresponding to the formation of  $\text{Ce}-\text{O H-CO}$  complexes are visible at higher wavenumbers (negative peak at  $3740\text{ cm}^{-1}$  and an adsorption at  $3660\text{ cm}^{-1}$ ). When the  $\text{Ce}_{0.9}\text{Zr}_{0.1}\text{O}_2$ -SCS was outgassed at  $450\text{ }^{\circ}\text{C}$  (Fig. 6B) the peak at  $2169\text{ cm}^{-1}$ , attributed to physisorbed CO, red shifted of to  $2150\text{ cm}^{-1}$  ( $\Delta\nu=24\text{ cm}^{-1}$ ), thus suggesting the presence of less energetically uniform adsorption sites with respect to the  $\text{Ce}_{0.9}\text{Zr}_{0.1}\text{O}_2$ -NP. The heat of adsorption decreases as the surface coverage increases, since stronger centres interact first with CO molecules [63]. CO was found to interact weakly with the (111)  $\text{CeO}_2$  surface, whereas CO chemisorption typically occurs on the more open (110) and (100) planes [29]. On the other hand, intense signals due to  $\text{Ce}^{4+}$  and  $\text{Zr}^{4+}$  ions can be observed at higher wavenumbers ( $2188$  and  $2177\text{ cm}^{-1}$ , respectively), likely due to the easier surface dehydroxylation and higher surface area of the  $\text{Ce}_{0.9}\text{Zr}_{0.1}\text{O}_2$ -SCS sample. This finding is in agreement with the low intensity signals appearing in the OH stretch region (inset). With both samples, interaction with CO was reversible in that, by letting samples thaw and then outgassing at room temperature for about 30 min, CO molecules were readily desorbed, in agreement with

the weakness of (electrostatic) interaction of this probe with either surface hydroxyls or metal cations.

### 3.5. Catalytic activity tests

The catalytic behaviour towards CO oxidation was tested in the  $150$ – $450\text{ }^{\circ}\text{C}$  temperature range. Fig. 7 shows the CO conversion to  $\text{CO}_2$  as a function of the reaction temperature achieved for the  $\text{Ce}_x\text{Zr}_{1-x}\text{O}_2$ -NP catalysts along with the uncatalyzed reaction (no catalyst). As a whole, the three nanostructured catalysts exhibit positive CO conversion trends for an increasing reaction temperature, and total oxidation of CO is completed around  $400\text{ }^{\circ}\text{C}$ . Better performances (in terms of  $T_{10\%}$ ,  $T_{50\%}$ , and  $T_{90\%}$  values) appear for the  $\text{Ce}_{0.9}\text{Zr}_{0.1}\text{O}_2$ -NP sample, rather than for  $\text{Ce}_{0.8}\text{Zr}_{0.2}\text{O}_2$ -NP and  $\text{Ce}_{0.7}\text{Zr}_{0.3}\text{O}_2$ -NP. A similar trend can be observed by considering the CO specific rates (data reported in Table 3) measured under a kinetically controlled regime, where both diffusive and mass-transfer phenomena are avoided. As a result, the  $\text{Ce}_{0.9}\text{Zr}_{0.1}\text{O}_2$ -NP appears to be the most active catalyst, as a consequence of its better redox properties and easier surface reducibility, as confirmed by both XPS and  $\text{H}_2$ -TPR analyses (*vide supra*, [8]). The high catalytic activity of ceria-zirconia nanocatalysts seems to be related to the presence of highly reactive (100) and (110) planes. For these comparable nanostructures, indeed, a direct correlation can be drawn between the catalytic activity and the relative abundance of the low index planes estimated by the XRD analysis (data reported in Table 1).

The partial substitution of  $\text{Ce}^{4+}$  ions (ionic radius of  $0.97\text{ \AA}$ ) for  $\text{Zr}^{4+}$  ( $0.84\text{ \AA}$ ) favours the creation of structural defects and oxygen vacancies in the ceria-zirconia lattice, thus inducing a distortion of the oxygen sublattice. On the other hand, the population of redox centres (namely,  $\text{Ce}^{3+}/\text{Ce}^{4+}$  pairs) decreases as the Zr-content increases [7]. Moreover, the mobility of electrons and lattice oxygens within the solid framework can be promoted at higher Ce-contents. Therefore, the incorporation of  $\text{Zr}^{4+}$  cations

**Table 3**  
CO oxidation activity results of catalysts.

Sample	$T_{10\%}$ ( $^{\circ}\text{C}$ )	$T_{50\%}$ ( $^{\circ}\text{C}$ )	$T_{90\%}$ ( $^{\circ}\text{C}$ )	Specific rate at $220\text{ }^{\circ}\text{C}$ ( $\text{mol m}^{-2}\text{ h}^{-1}$ ) $\times 10^3$	Specific rate at $220\text{ }^{\circ}\text{C}$ ( $\text{mol g}^{-1}\text{ h}^{-1}$ ) $\times 10^3$
$\text{Ce}_{0.9}\text{Zr}_{0.1}\text{O}_2$ -NP	224	248	288	40.5	80.9
$\text{Ce}_{0.8}\text{Zr}_{0.2}\text{O}_2$ -NP	253	302	362	8.8	17.7
$\text{Ce}_{0.7}\text{Zr}_{0.3}\text{O}_2$ -NP	241	285	333	2.7	10.7
$\text{Ce}_{0.9}\text{Zr}_{0.1}\text{O}_2$ -NP/FAU	229	266	293	<sup>a</sup> 69.0 <sup>a</sup>	137.1 <sup>a</sup>
$\text{Ce}_{0.9}\text{Zr}_{0.1}\text{O}_2$ -M	227	271	330	0.8	93.2
$\text{Ce}_{0.9}\text{Zr}_{0.1}\text{O}_2$ -SCS	249	288	322	0.7	14.1

<sup>a</sup> Value calculated considering the specific surface area and the weight of the active phase dispersed over the FAU-type zeolite.

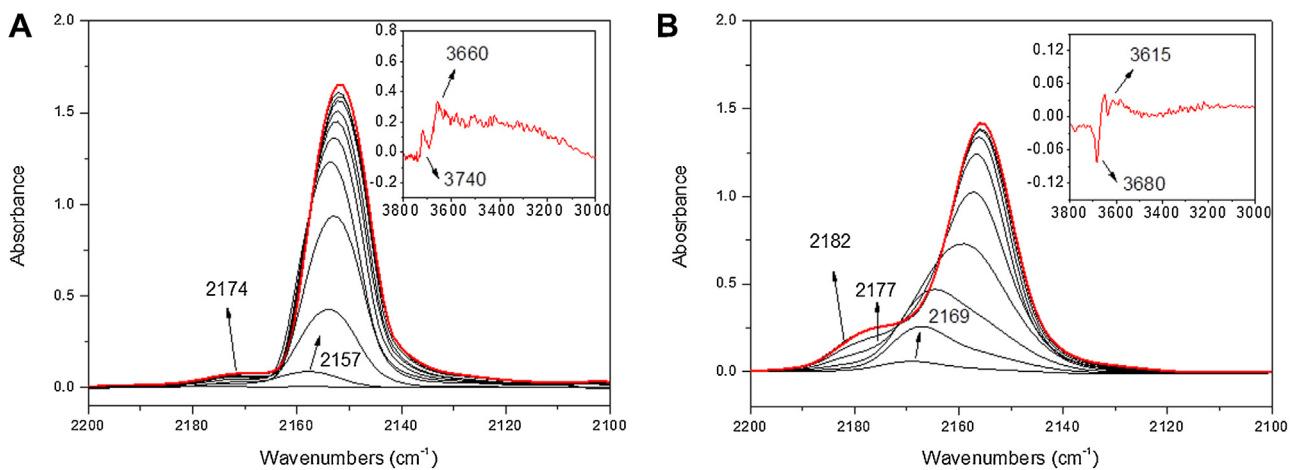


**Fig. 6.** FT-IR difference spectra, recorded after dosing CO (equilibrium pressure in the 0.01–20 mbar range) at nominal  $-196^{\circ}\text{C}$  on  $\text{Ce}_{0.9}\text{Zr}_{0.1}\text{O}_2$ -SCS sample outgassed at  $150^{\circ}\text{C}$  (Section A) and  $450^{\circ}\text{C}$  (Section B). Insets: same difference spectra in the OH stretching region (after dosing 20 mbar).

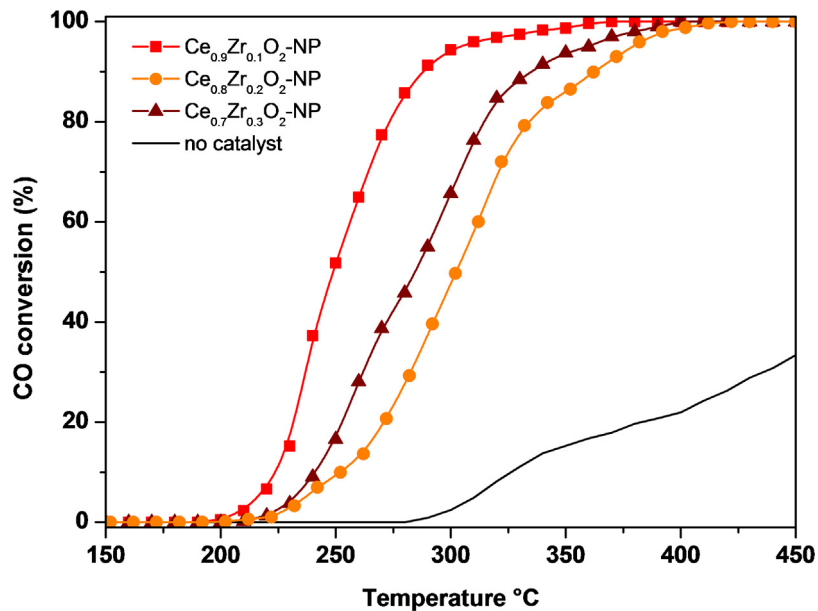


**Fig. 7.** CO to  $\text{CO}_2$  conversion versus temperature over the  $\text{Ce}_x\text{Zr}_{1-x}\text{O}_2$ -NP catalysts.

into the  $\text{CeO}_2$  lattice does not have a direct beneficial effect on CO oxidation for catalytic materials calcined at low/mild temperature, since it reduces the surface redox-active centres, which are directly dependent on the Cerium surface density. Thus, the best compromise between the structural defects and redox-active centers can be obtained for the  $\text{Ce}_{0.9}\text{Zr}_{0.1}\text{O}_2$ -NP catalyst.

Fig. 8 shows CO oxidation as a function of temperature over ceria-zirconia catalysts (atomic ratio  $\text{Ce}/\text{Zr}=0.9$ ) to study the role of topological and textural properties on the catalytic performance. The FAU-type support was also tested and showed comparable conversion values with those achieved in the absence of catalyst. All catalysts exhibit positive CO conversion trends for an increasing reaction temperature and the best results are obtained with the  $\text{Ce}_{0.9}\text{Zr}_{0.1}\text{O}_2$ -NP catalyst, despite its poor textural properties in terms of specific surface area and total pore volume (Table 1). The highest CO oxidation activity of the latter catalyst, indeed, is mainly related to the richer population of carbonate-like species on more open and reactive surfaces, namely, (110) and (100) ones [29]. According to the literature, carbonate species associated with  $\text{Ce}^{4+}/\text{Ce}^{3+}$  cations are among the reaction intermediates in CO oxi-

dation process [13]. As it is known, oxygen spillover at catalyst surface contributes to the CO oxidation [66,67], and an abundant presence of surface polycarbonates, stable at high temperature, has a beneficial effect on the reactivity of ceria-zirconia nanocatalysts. The high stability of polycarbonate species on the catalyst surface has been confirmed by FT-IR analysis on the  $\text{Ce}_{0.9}\text{Zr}_{0.1}\text{O}_2$ -NP sample after CO oxidation reaction (up to  $450^{\circ}\text{C}$ ), as shown in Fig. S5 (Supporting Information). On the other hand, the least active catalyst seems to be the  $\text{Ce}_{0.9}\text{Zr}_{0.1}\text{O}_2$ -SCS, with the highest amount of stable (111) planes. These findings are in agreement with previous works [8,47], according to which ceria-based catalysts, exhibiting highly reactive planes, show promising catalytic activities for Diesel soot combustion despite their low surface area and pore volume.

The CO specific rates for the prepared catalysts, Fig. S6 (Supporting Information), confirm that the  $\text{Ce}_x\text{Zr}_{1-x}\text{O}_2$ -NPs are more active than high-surface area catalysts, as already detailed in Table 3.

Interesting results are attained with the  $\text{Ce}_{0.9}\text{Zr}_{0.1}\text{O}_2$ -NP/FAU catalyst, even though the amount of the active phase (50 wt.%  $\text{Ce}_{0.9}\text{Zr}_{0.1}\text{O}_2$ -NP on the surface of FAU) is lower, thus confirming the beneficial role of the zeolite-type support. From a TPD-O<sub>2</sub>

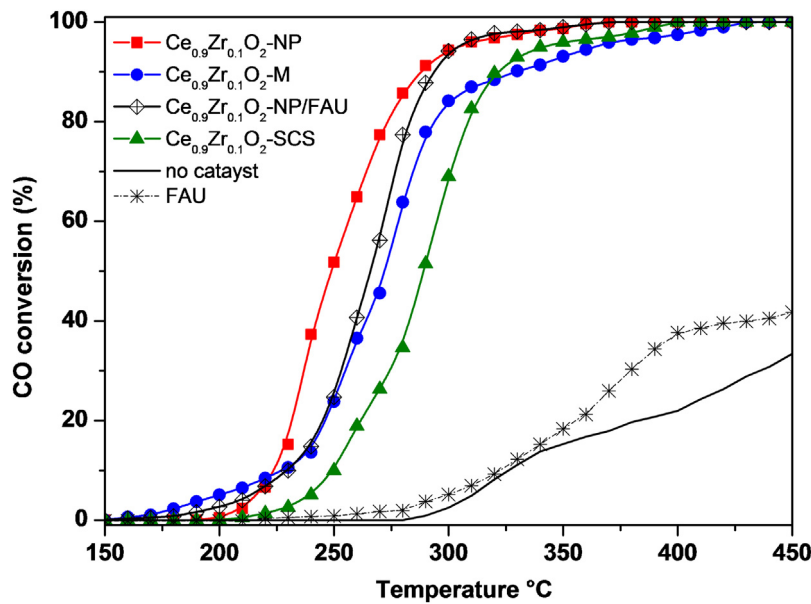


Fig. 8. CO to  $\text{CO}_2$  conversion versus temperature over the ceria-zirconia catalysts (atomic ratio  $\text{Ce}/\text{Zr} = 0.9$ ) and pure FAU-type zeolite.

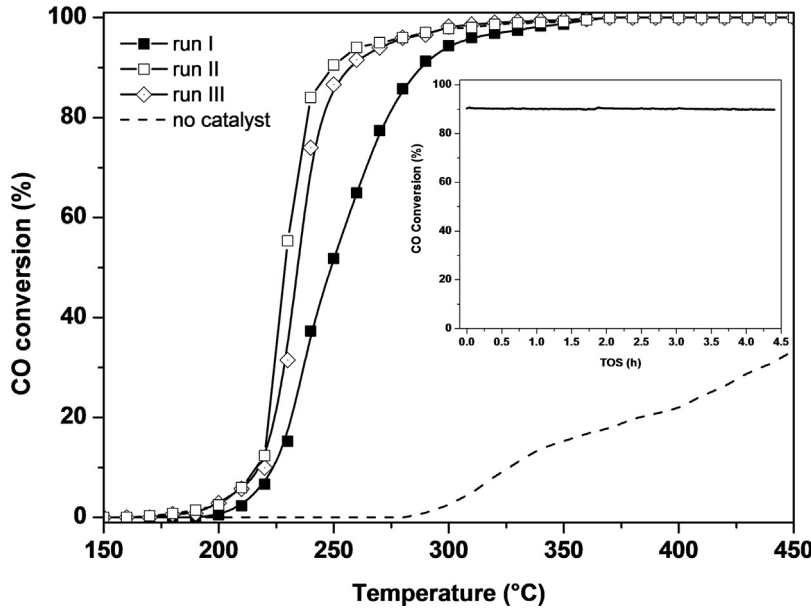


Fig. 9. Stability study of the  $\text{Ce}_{0.9}\text{Zr}_{0.1}\text{O}_2\text{-NP}$  catalyst for three successive catalytic cycles. Inset: effect of time-on stream on the catalytic activity of the  $\text{Ce}_{0.9}\text{Zr}_{0.1}\text{O}_2\text{-NP}$  catalyst at constant temperature (namely, at  $288^\circ\text{C}$ , corresponding to  $T_{90\%}$ ).

analysis operated on the pure FAU-type zeolite, oxygen desorption occurs almost completely before ca.  $200^\circ\text{C}$  (data not reported for the sake of brevity). Therefore, the increased activity of the  $\text{Ce}_{0.9}\text{Zr}_{0.1}\text{O}_2\text{-NP/FAU}$  catalyst (see Table 3 and Fig. S6) can be ascribed to a better dispersion of the nanopolyhedra on the FAU surface, with a high accessibility of the reactive planes, rather than to the oxygen availability at the catalyst surface.

In order to test the  $\text{Ce}_{0.9}\text{Zr}_{0.1}\text{O}_2\text{-NP/FAU}$  catalyst with the same active phase amount (namely, 0.1 g of  $\text{Ce}_{0.9}\text{Zr}_{0.1}\text{O}_2\text{-NP}$ ), a two-fold catalyst weight was used (Fig. S7, Supporting Information). In this way, the active phase weight per unit of CO flow rate (commonly referred as W/F), used in the other activity tests, was retained. As expected, a higher amount of  $\text{Ce}_{0.9}\text{Zr}_{0.1}\text{O}_2\text{-NP}$  increases the CO conversion, due to the larger number of reactive (100) and (110) surfaces, and exceeds the catalytic performances of the unsupported  $\text{Ce}_{0.9}\text{Zr}_{0.1}\text{O}_2\text{-NP}$ , due to their improved accessibility.

The conversion curve of the  $\text{Ce}_{0.9}\text{Zr}_{0.1}\text{O}_2\text{-M}$  shows a lower slope (especially at high temperature), thus suggesting that mass-transport limitations (e.g. Knudsen diffusion) takes place in the mesoporous framework. Finally, the worst performances were obtained for the  $\text{Ce}_{0.9}\text{Zr}_{0.1}\text{O}_2\text{-SCS}$  catalyst, thus confirming the key role played by the structural properties of the nanocatalysts for this reaction.

A more technological way to express the intrinsic activity is to calculate it based on the mass of catalyst, instead of referring to the specific surface. Hence, the catalyst loading on a support, expressed on a weight basis, is the parameter that is optimized in reactor design. Based on this criterion, from the last column of Table 3, one can see that  $\text{Ce}_{0.9}\text{Zr}_{0.1}\text{O}_2\text{-NP/FAU}$  is the best catalyst, i.e. if the  $\text{Ce}_{0.9}\text{Zr}_{0.1}\text{O}_2\text{-NP}$  active phase is well dispersed. The  $\text{Ce}_{0.9}\text{Zr}_{0.1}\text{O}_2\text{-NP}$  alone is still almost six times more active than  $\text{Ce}_{0.9}\text{Zr}_{0.1}\text{O}_2\text{-SCS}$ . Finally, the activity of  $\text{Ce}_{0.9}\text{Zr}_{0.1}\text{O}_2\text{-M}$  is remark-

able at the temperatures at which it was estimated ( $220^{\circ}\text{C}$ ) but, as mentioned above, it exhibits a lower activity at increasing temperatures (see Fig. 8), thereby having a limited range of applicability.

For practical application purposes, catalytic stability is an important feature for catalytic materials used in industrial applications. Therefore, several activity tests have been performed in order to evaluate the surface stability of the prepared catalysts. Experiments were conducted with a continuous supply of CO to the  $\text{Ce}_{0.9}\text{Zr}_{0.1}\text{O}_2-\text{NP}$  catalyst for more than 4 h at constant temperature (namely at  $288^{\circ}\text{C}$ , corresponding to  $T_{90\%}$ ) (Inset to Fig. 9). As a result, the catalyst exhibited high stability and no deactivation occurred over that time span. Comparable performances have been obtained for the other ceria-zirconia catalysts (data not reported for the sake of brevity). Fig. 9 shows three catalytic cycles of the  $\text{Ce}_{0.9}\text{Zr}_{0.1}\text{O}_2-\text{NP}$  catalyst, as a function of temperature, for each heating run kept at  $450^{\circ}\text{C}$  for 1 h. Interestingly, the CO conversion values increase after the “run I”, because of the formation of stronger Lewis acidic sites generated during the first heating by surface de-hydroxylation, as revealed by IR analysis.

#### 4. Conclusions

As a whole, it has been observed that the catalytic performances for CO oxidation over ceria-zirconia catalysts mainly depend on the presence of highly reactive (100) and (110) surfaces, thus confirming the structure-sensitivity for this prototypical reaction. In addition, it has been shown that the abundant population of energetically stable bi- and polidentate carbonates on more open and reactive surfaces has a beneficial effect on the reactivity of ceria-zirconia nanocatalysts ( $\text{Ce}_x\text{Zr}_{1-x}\text{O}_2-\text{NP}$ ). On the other hand, the least active catalyst was the  $\text{Ce}_{0.9}\text{Zr}_{0.1}\text{O}_2-\text{SCS}$ , with the highest amount of stable (111) planes. The best compromise between the structural defects and redox-active centres was observed for the most active catalyst, namely the  $\text{Ce}_{0.9}\text{Zr}_{0.1}\text{O}_2-\text{NP}$ . The latter catalyst exhibited superior catalytic performances compared to similar nanocatalysts with higher Zr-contents (namely,  $\text{Ce}_{0.8}\text{Zr}_{0.2}\text{O}_2-\text{NP}$  and  $\text{Ce}_{0.7}\text{Zr}_{0.3}\text{O}_2-\text{NP}$ ). Interesting results were attained with the  $\text{Ce}_{0.9}\text{Zr}_{0.1}\text{O}_2-\text{NP}/\text{FAU}$  catalyst, thus confirming the beneficial role of the zeolite-type support to disperse the active phase. Conversely, lower CO conversion values were obtained for the high-surface-area catalysts ( $\text{Ce}_{0.9}\text{Zr}_{0.1}\text{O}_2-\text{M}$  and  $\text{Ce}_{0.9}\text{Zr}_{0.1}\text{O}_2-\text{SCS}$ ), thus showing the key role played by the structural properties of ceria-zirconia catalysts for the CO oxidation reaction.

#### Acknowledgments

The Ministero dell'Università e della Ricerca (MIUR) (grant number: RBFR12LS6M 001) is acknowledged for sponsoring this research activity (FIRB—Futuro in Ricerca 2012). Authors thank Prof. Fabrizio Giorgis and Dr. Alessandro Virga (Politecnico di Torino, Italy) for Raman measurements.

#### Appendix A. Supplementary data

Supplementary data associated with this article can be found, in the online version, at <http://dx.doi.org/10.1016/j.apcatb.2016.02.023>.

#### References

- [1] A. Trovarelli, P. Fornasiero, *Catalysis by Ceria and Related Materials*, 2nd ed., Imperial College Press, London, 2013.
- [2] R.J. Heck, *Catalytic Air Pollution Control: Commercial Technology*, 3rd ed., Wiley-VCH, Hoboken, New Jersey, 2006, pp. 1–518.
- [3] G. Ertl, H. Knözinger, F. Schüth, J. Weitkamp, *Handbook of Heterogeneous Catalysis*, 2nd ed., Wiley-VCH, Weinheim, 2008, pp. 2274–2344.
- [4] D. Duprez, F. Cavani, *Handbook of Advanced Methods and Processes in Oxidation Catalysis*, Imperial College Press, London, 2014.
- [5] M. Thammachart, V. Meeyoo, T. Risksomboon, S. Osuwan, *Catal. Today* 68 (2001) 53–61.
- [6] R. Burch, *Catal. Rev.* 46 (2004) 271–233.
- [7] E. Aneggi, M. Boaro, C. de Leitenburg, G. Dolcetti, A. Trovarelli, *J. Alloy Compd.* 408–412 (2006) 1096–1102.
- [8] M. Piumetti, S. Bensaïd, N. Russo, D. Fino, *Appl. Catal. B* 180 (2016) 271–282.
- [9] K. An, G.A. Somorjai, *Catal. Lett.* 145 (2015) 233–248.
- [10] J.C. Vedrine, *Appl. Catal. A* 474 (2014) 40–50.
- [11] F. Volkenshtein, *The Electronic Theory of Catalysis on Semiconductors*, Pergamon Press, New York, 1963.
- [12] R.A. van Santen, M. Neurock, *Molecular Heterogeneous Catalysis*, Wiley-VCH, Verlag, 2006 (p. 474).
- [13] Z.L. Wu, M.J. Li, S.H. Overbury, *J. Catal.* 285 (2012) 61–73.
- [14] N. Russo, D. Fino, G. Saracco, V. Specchia, *Catal. Today* 117 (2006) 214–219.
- [15] H.J. Freund, G. Meijer, M. Scheffler, R. Schogol, M. Wolf, *Angew. Chem. Int. Ed.* 50 (2011) 10064–10094.
- [16] S. Royer, D. Duprez, *ChemCatChem* 3 (2011) 24–65.
- [17] E. Aneggi, J. Ilorca, M. Boaro, A. Trovarelli, *J. Catal.* 234 (2005) 88–95.
- [18] Z.M. Tana, M. Zhang, J. Li, H. Li, Y. Li, W. Shen, *Catal. Today* 148 (2009) 179–183.
- [19] X.W. Liu, K.B. Zhou, L. Wang, B.Y. Wang, Y.D. Li, *J. Am. Chem. Soc.* 131 (2009) 3140–3141.
- [20] L. Yan, R.B. Yu, J. Chen, X.R. Xing, *Cryst. Growth Des.* 8 (2008) 1474–1477.
- [21] Y.J. Guan, E.J.M. Hensen, Y. Liu, H.D. Zhang, Z.C. Feng, C. Li, *Catal. Lett.* 137 (2010) 28–34.
- [22] K.S. Lin, S. Chowdhury, *Int. J. Mol. Sci.* 11 (2010) 3226–3251.
- [23] W.Q. Han, W. Wen, J.C. Hanson, X.W. Teng, N. Marinkovic, J.A. Rodriguez, *J. Phys. Chem. C* 113 (2009) 21949–21955.
- [24] T.K. Sau, A.L. Rogach, *Complex-Shaped Metal Nanoparticles: Bottom-Up Syntheses and Applications*, Wiley-VCH, 2012.
- [25] Z.L. Wang, X. Feng, *J. Phys. Chem. B* 107 (2003) 13563–13566.
- [26] B.T. Teng, S.Y. Jiang, X.W. Guo, J.H. Yuan, M.F. Luo, *Acta Chim. Sin.* 67 (2009) 2765–2772.
- [27] M. Nolan, *J. Phys. Chem. C* 113 (2009) 2425–2432.
- [28] C. Müller, B. Paulus, K. Hermansson, *Surf. Sci.* 603 (2009) 2619–2623.
- [29] M. Huang, S. Fabris, *J. Phys. Chem. C* 112 (2008) 8643–8648.
- [30] D.O. Scanlon, N.M. Galea, B.J. Morgan, G.W. Watson, *J. Phys. Chem. C* 113 (2009) 11095–11103.
- [31] M.K. Alam, F. Ahmed, K. Nakamura, A. Suzuki, R. Sahnoun, H. Tsuboi, M. Koyama, N. Hatakeyama, A. Endou, H. Takaba, C.A. Del Caprio, M. Kubo, A. Miyamoto, *J. Phys. Chem. C* 113 (2009) 7723–7727.
- [32] Z. Cheng, B.J. Sherman, C.S. Lo, *J. Chem. Phys.* 138 (2013), 014702-1–12.
- [33] M. Nolan, J.E. Fearon, G.W. Watson, *Solid State Ionics* 177 (2006) 3069–3074.
- [34] G. Pacchioni, *ChemPhysChem* 4 (2003) 1041–1047.
- [35] M. Nolan, S.C. Parker, G.W. Watson, *Surf. Sci.* 595 (2005) 223–232.
- [36] J. Cejka, A. Corma, S. Zones, *Zeolites and Catalysis: Syntesis, Reactions and Applications*, Wiley-VCH, Weinheim, 2010.
- [37] Y. Liu, C. Wen, Y. Guo, G. Lu, Y. Wang, *J. Mol. Catal. A: Chem.* 316 (2010) 59–64.
- [38] A. Civera, M. Pavese, G. Saracco, V. Specchia, *Catal. Today* 83 (2003) 199–211.
- [39] N. Russo, D. Fino, G. Saracco, V. Specchia, *Catal. Today* 117 (2006) 214–219.
- [40] E. Aneggi, C. de Leitenburg, G. Dolcetti, A. Trovarelli, *Catal. Today* 114 (2006) 40–47.
- [41] A.M. Hernandez-Gimenez, L.P. dos Santos Xavier, A. Bueno-Lopez, *Appl. Catal. A* 462–463 (2013) 100–106.
- [42] Database of Zeolite Structures, <http://www.iza-structure.org/>.
- [43] M. Hussain, N. Russo, G. Saracco, *Chem. Eng. J.* 166 (2011) 138–149.
- [44] G. Wulff, Z. Kristallogr. Mineral 34 (1901) 449–530.
- [45] P. Ji, J. Zhang, F. Chen, M. Anpo, *J. Phys. Chem. C* 112 (2008) 17809–17813.
- [46] G. Zhang, Z. Shen, M. Liu, C. Guo, P. Sun, Z. Yuan, B. Li, D. Ding, T. Chen, *J. Phys. Chem. B* 110 (2006) 25782–25790.
- [47] M. Piumetti, S. Bensaïd, N. Russo, D. Fino, *Appl. Catal. B* 165 (2015) 742–751.
- [48] M. Piumetti, S. Bensaïd, N. Russo, *SAE Tech. Pap.* 24 (2015) 2514.
- [49] A. Galtayries, R. Sporken, J. Riga, G. Blanchard, R. Caudano, *J. Electron. Spectrosc. Relat. Phenom.* 88–91 (1998) 951–956.
- [50] B.M. Reddy, A. Khan, Y. Yamada, T. Kobayashi, S. Loridant, J.-C. Volta, *J. Phys. Chem. B* 107 (2003) 5162–5167.
- [51] P.C. Wong, Y.S. Li, K.A.R. Mitchell, *Surf. Rev. Lett.* 2 (3) (1995) 297–303.
- [52] S. Suohonen, M. Valden, M. Hietikko, R. Laitinen, A. Savimäki, M. Häkkinen, *Appl. Catal. A* 218 (2001) 151–160.
- [53] Y. Li, Z. Wei, F. Gao, L. Kovarik, R.A.L. Baylon, C.H.F. Peden, Y. Wang, *ACS Catal.* 5 (2015) 3006–3012.
- [54] O.H. Laguna, M.A. Centeno, F. Romero-Sarria, J.A. Odriozola, *Catal. Today* 172 (2011) 118–123.
- [55] L.F. Nascimento, R.F. Martins, R.F. Silva, P.C. de Sousa Filho, O.A. Serra, *Reac. Kinet. Mech. Catal.* 111 (2014) 149–165.
- [56] W.Y. Hernandez, M.A. Centeno, F. Romero-Sarria, J.A. Odriozola, *J. Phys. Chem. C* 113 (2009) 5629–5635.
- [57] S. Agarwal, X. Zhu, E.J.M. Hensen, L. Lefferts, B.L. Mojet, *J. Phys. Chem. C* 118 (2014) 4131–4142.
- [58] Agarwal, L. Lefferts, B.L. Mojet, *ChemCatChem* 5 (2013) 479–489.
- [59] E. Finocchio, M. Daturi, C. Binet, J.C. Lavalle, G. Blanchard, *Catal. Today* 52 (1999) 55–63.
- [60] M. Piumetti, M. Armandi, E. Garrone, B. Bonelli, *Microporous Mesoporous Mater.* 164 (2012) 111–119.

- [61] A.A. Davydov, Infrared Spectroscopy of Adsorbed Species on the Surface of Transition Metal Oxides, Wiley Chichester, UK, 1990, pp. 38.
- [62] K.I. Hadjiivanov, G.N. Vayssilov, *Adv. Catal.* 47 (2002) 307–511.
- [63] B. Bonelli, M. Cozzolino, R. Tesser, M. Di Serio, M. Piumetti, E. Garrone, E. Santacesaria, *J. Catal.* 246 (2007) 293–300.
- [64] C. Binet, M. Daturi, J.C. Lavalle, *Catal. Today* 50 (1999) 207–225.
- [65] A. Penkova, O.H. Laguna, M.A. Centeno, J.A. Ordiozola, *J. Phys. Chem. C* 116 (2012) 5747–5756.
- [66] J.M. Thomas, W.J. Thomas, *Principles and Practice of Heterogeneous Catalysis*, 2nd ed., Wiley-VCH, Verlag, 2015, pp. 113–126.
- [67] J.Y. Luo, M. Meng, X. Li, X.G. Li, Y.Q. Zha, T.D. Hu, Y.N. Xie, J. Zhang, *J. Catal.* 254 (2008) 310–324.